Assessment and mitigation of wall light reflection in ITER by ray tracing

Shin Kajita

Institute of Materials and Systems for Sustainability,

*Nagoya University, Nagoya 464-8603, Japan**

Evgeny Veshchev, Maarten De Bock, Robin

Barnsley, Manfred von Hellemann, Michael Walsh

ITER Organization, Route de Vinon-sur-Verdon,

CS 90 046, 13067 St. Paul Lez Durance Cedex, France

(Dated: August 7, 2017)

Abstract

In ITER, reflection of photons on vacuum vessel will make parasitic signals (stray light) for optical diagnostics. In this study, to estimate and mitigate the effect of the stray light in ITER in a systematic manner, ray transfer matrix was constructed based on ray tracing calculations for divertor impurity monitor and charge exchange recombination spectroscopy (CXRS). It is shown that the allocation of the sources around the strike point and the X-point, where the emission is strong, is important for the model used to build the transfer matrix to effectively mitigate the stray light. The origin of the stray light for the core CXRS is investigated, and a case study to subtract the stray light is shown.

PACS numbers:

*Electronic address: kajita.shin@nagoya-u.jp

I. INTRODUCTION

Disturbance of the measurement by the reflection of photons in vacuum vessel of fusion experimental reactor has been identified in various optical diagnostics. For example, in DIII-D [1], it was shown that the stray light can be $\sim 50\%$ of the actual signal for viewing cords not directly seeing the divertor region. In JET ITER-like wall experiments, it was demonstrated that the stray light level can be 100-500% of the signal from the scrape off layer (SOL) from detailed spectrum shape analysis [2, 3]. In ITER, the stray light issue can be more serious than present tokamak devices, because the wall is fully metal, which has higher reflectance than carbon based materials, and the emission profiles will have higher contrast.

In ITER H-alpha spectroscopy, it was shown that brighter divertor emission can form much greater stray light than the actual signal [4]. In charge exchange recombination spectroscopy (CXRS), the attenuation of beam can be three orders of magnitude. In addition to an increase in the photon noise [5], bright divertor emission may lead to saturation of the detector, and the CXRS signal in the edge region may be considerable superimposed on the weak core signal by reflection [6]. On infrared thermography, it was pointed out from the ray tracing simulation that the first wall surface temperature can be overestimated by 100% and the divertor material temperature in colder private region can be overestimated by 85% [7, 8].

To mitigate the influence of stray light in ITER, the performance of several viewing dump has been assessed [4], and the method to obtain the original signal by using inverse method for spectrum shape has been tried for synthetic diagnostic [9]. It is necessary further develop synthetic optical diagnostics and assess and develop the method to mitigate the stray light. In this study, to estimate and mitigate the effect of the stray light in ITER, ray tracing simulations are performed using a software LightTools [10]. Since the ray tracing runs take long time, assessments have been conducted for only limited cases until now. In this study, we build ray transfer matrix [11] and use it for assessment and mitigation of the stray light for divertor impurity monitor (DIM) and CXRS. It is shown that usage of ray transfer matrix can be a powerful tool that can be implemented to the data analysis procedure, since it does not require further time consuming ray tracing runs.

II. MODEL

Ray tracing calculations were conducted using the commercial ray tracing software LightTools. Details of the model were explained in previous works [6, 12]; here, models used are explained briefly. Computer aided design (CAD) data of ITER wall and divertor etc. and emission profiles were installed to the LightTools model for the simulation. For DIM, because the emission source is toroidally uniform, a 20° (1/18th part) toroidal sector model was used. For CXRS, the emission along the diagnostic beam should be treated, 360° full model was used. In this study, since we focused on the stray light formed inside the vacuum vessel, not inside optics, we omitted actual collection optics and used a pinhole camera configuration. We used backward ray tracing, in which rays are traced from the receiver to the vacuum vessel through the pinhole.

Figure 1(a) and (b) shows a schematic drawing of the field of views (FoVs) used for DIM and CXRS, respectively. Four FoVs from upper port plug, equatorial port plug, and two under divertor dome port for high field side (HFS) and low field side (LFS) are used. We call them UPP, EPP, DP-HFS, and DP-LFS in this study. For CXRS, we used a FoV for core region from the upper port plug, which covers $r/a = \rho < 0.7$. One of the important parameters for simulations is the reflection property of walls. We used the combination of specular and diffuse reflection. We assumed Gaussian profile of 6° in half-width for specular reflection [13], and a Lambertian profile is used for diffuse reflection. We assume that the reflectance of divertor and first wall was 50% [12] when we consider reflection, and we change the ratio of specular and diffuse reflectance, R_s/R_d.

To run calculations, we have to install the emission profiles to the model. We use toroidal shaped sources based on the emission profiles calculated using SOLPS4.3 code (B2-Eirene) and DIVIMP [14]. Since the number of cell is more than 3000 in the SOLPS4.3 mesh used, it takes long time for a calculation in the lightTools if we use them all. Thus, previously, we decreased the number of the installed sources to the LightTools model by averaging the emission profile [12]. For practical application, there is a way to use transfer matrix, which can calculate radiance profiles (signal intensity at the receiver) without new installation of sources and further ray tracing runs.

Since a radiance profile on a receiver can be expressed with the summation of contributions from all the sources, the radiance profile on kth receiver $I^k(x)$ can be expressed

as

$$I^k(x) = \sum_i a_i J_i^k(x), \tag{1}$$

where $J_i^k(x)$ is the radiance profile on kth receiver from ith source when the source has a unit power, x corresponds to the relative location on the receiver, and a_i is a coefficient, which corresponds to the intensity of the ith source. We can calculate the ray transfer matrix $J_i^k(x)$ from ray tracing calculations. When the emission profile is given in a_i, we can calculate the radiance profile at the kth receiver [11]. To assess the stray light for the divertor impurity monitor and CXRS, we prepared the necessary matrices and use them to obtain the radiance profile in this study.

III. DIVERTOR IMPURITY MONITOR

A. Validation of transfer matrix

Figure 2(a) shows the profile of calculated He I emission power at 587 nm (2^3P-3^3D) used in this study. The carbon-free ITER divertor with Ne seeding is selected. The calculation is characterized by the peak power loading on the target (10 MW/m^2) and the total power radiated from the SOL and divertor (43 MW). The emission is strong in the private region especially around the X-point and strike points. Figure 2(b) shows a comparison between the results from the direct ray trace calculation and the transfer matrix. Dotted lines correspond to the direct ray tracing calculation and solid lines represent the ones from the transfer matrix, and the cases with and without reflections are shown. When reflection was taken into account, we assumed that $R_d/R_s = 25/25$ here. It is seen that dotted lines well agree with the solid lines and the profiles are well reproduced. Around the peak, transfer matrix calculations were slightly ($\sim$10%) higher than the direct ray tracing calculation. This minor difference could be originated from the averaging processes of the sources for the direct calculations. Hereafter, transfer matrix is used to calculate the radiance profile for synthetic signal.

B. Impurity profiles

Figure 3(a-d) shows the calculated radiance profiles of He I (587 nm) for DP-LFS, DP-HFS, EPP, and LPP receivers, respectively. In addition to the case without reflection, i.e., $R_d/R_s = 0/0$, three cases with reflection at $R_d/R_s = 1/49$, 25/25, and 49/1 are shown. We built four transfer matrices with different optical property for each receiver. On DP receivers, when $R_d/R_s = 1/49$, strong reflection peaks appeared at ∼50 mm on DP-LFS and -20 mm on DP-HFS. The peak intensity was one order of magnitude higher than the case without reflection when the specular reflection component was high, and the intensities decreased with the increase of R_d/R_s. It is likely that the peak was originated from the reflection of the emission around X-point.

For EPP receiver, two peaks around 0 and 100 mm were observed. These were from the X-point and the HFS strike point, respectively. When the reflection was taken into account, the peak intensity, especially the one at 100 mm, increased, and the background emission increased as well. The background level increased by increasing R_d/R_s. In Fig. 3(d), it is seen that the UPP receiver has a peak around the center from the X-point without reflection. When considering the reflection, two small peaks appeared around -50 and 30 mm. The position of the peaks altered slightly when changing R_d/R_s.

To investigate the origin of the peaks observed on DP receivers at $R_d/R_s = 1/49$, we conducted a ray path analysis focusing around the peaks. Figure 4(a) and (b) shows the major ray paths which contributed to the reflection for DP-LFS and DP-HFS, respectively. It is seen that all the rays were terminated around the X-point. This suggested that one or two reflection from the X-point formed the peaks around 50 mm for DP-LFS and -20 mm for DP-HFS. Concerning the rays to DP-LFS receiver, they hit on the inner target plate, the dome, and the outer target plate. On the other hand, as for DP-HFS receiver, no major rays hit on the outer target. Because the specular wall was assumed, the difference could be originated from the subtle difference in the orientation of target plates. Previously, since no strong emission existed around the X-point, the stray light did not form new peaks for H_α and Be cases [12]. The present calculation indicates that there is a possibility that emission from the X-point makes phantom peak by reflection in some cases. In the next section (Sec. III C), we discuss the mitigation of those reflections by using ray tracing analysis.

C. Mitigation using transfer matrix

It has been shown recently that transfer matrix calculated using the ray tracing simulation can be used to mitigate the stray light [11]. The original emission profile can be reconstructed using the transfer matrix considering the influence of the stray light. Here, we investigate the accuracy of the reconstruction with using three models having a difference in the source allocation.

Figure 5(a) shows schematics of the used models: case (i), (ii), and (iii). The numbers of sources, N_s, in cases (i)-(iii) are 30, 90, and 90, respectively. In case (iii), the sources around the strike point and the X-point are allocated in more detailed manner compared to case (ii). In the fitting process to obtain the set of a_i, it is necessary to define a function to be minimized; following function was used

$$error = \sum_{k=1}^{4} \frac{\sqrt{\sum_j (S_j^k - I_j^k)^2}}{\sum_j S_j^k}, \tag{2}$$

where S_j^k and I_j^k represent the synthetic and calculated radiance profiles, respectively, for jth line of sight for kth FoV.

Comparisons between the synthetic and calculated radiances profiles are shown in Figs. 5(b-d). In this comparison, we assumed $R_d/R_s = 25 : 25$. Green solid lines are the synthetic profiles and red solid, blue solid, and black dotted lines are calculated profiles for cases (i)-(iii), respectively. In case (i), where $N_s = 30$, differences were identified at various positions. Especially, for EPP receiver, the two peaks were not reproduced well. When we increased N_s, a better agreement was obtained, but the two peaks on the EPP receivers were not reproduced well in case (ii). When improving the allocation of sources around the strike point and the X-point, the agreement was improved in case (iii). The results indicated that the sources allocated around the strike point and X-point, where the emission is strong, are crucial for the reconstruction.

To check whether the stray light was actually reduced by the above process, we reconstruct the emission without reflection using the obtained a_i and transfer matrices without reflection. Comparisons between the synthetic profiles and reconstructed profiles without reflection in cases (i)-(iii) for DP-LFS, DP-HFS, EPP, and UPP receivers are shown in Fig. 6(a)-(d), respectively. It is seen that the deviation from the synthetic signal was improved from case (i) to case (iii).

Figure 7 shows the error of the each receiver as defining the error, Er, as

$$Er = \frac{\sqrt{\sum_j (S_j - I_j)^2}}{\sum_j S_j}. \tag{3}$$

Before mitigation, Er were comparable or large than 100%. Especially on DP receivers, Er exceeded 100%. After the mitigation method was applied, Er decreased significantly for all the receivers. The error decreased from case (i) to case (iii); for case (iii), Er decreased by more than an order of magnitude or became comparable to 10%. In this study, the sources were allocated manually; the error could be decreased further if we optimized the position of the sources with considering the equilibrium field in actual cases.

On the other hand, we should note that the difference in the optical property was not taken into account in the present study. As shown in Fig. 3, the phantom peak intensity can be altered by the reflection property. When the actual reflection property does not match with the one used to calculate the transfer matrix, the error would be increased. Recently, the measurement of the bidirectional reflectance distribution function (BRDF) of plasma facing material has been started [15]. It is of importance to implement the reflection property closer to the actual ones in the model when we calculate the transfer matrix.

IV. CHARGE EXCHANGE RECOMBINATION SPECTROSCOPY

In CXRS, there are three error sources taken care of associated with the reflection: (i) influence of the reflected active CXRS from the edge of the plasma that could overlap with the weaker active CXRS in the core of the plasma, (ii) disturbance of the CXRS spectrum by the emission from the divertor region (cold component), and (iii) increase in the noise by the reflected continuum radiation. There is a possibility that stray light of the item (i) can be mitigated or removed in the data analysis procedure. First, we determine the origin of the stray light for the FoV around the core and demonstrate to eliminate the stray light by a fitting procedure.

A. Origin of stray light

To help the analysis procedure, we investigated the stray light sources in various cases. Mainly, the signals around the core are contaminated. Here, we investigate the contribution

of the reflected CXRS signal at different positions on the chord at $\rho \sim 0.05$. A 3d full toroidal model was used, and the source was separated to 10 sources: ρ=0-0.1, 0.1-0.2, 0.2-0.3, 0.3-0.4, 0.4-0.5, 0.5-0.6, 0.6-0.7, 0.7-0.8, 0.8-0.9, and 0.9-1.0. The power of the sources were set to be 1 W, and transfer matrix for the sources to the receivers were constructed. Then, considering the intensity of the sources in the high and low density scenario shown in [6], the contribution of the stray light from each position to some specific position (here ρ=0.5) was assessed. Figure 8 shows the stray light ratio to the signal at ρ=0.05 originated from different positions from ρ=0.15 to 0.95. It is seen that the contribution to the stray light is mainly from the edge regions; this is because the signal intensity is significantly higher in those region, though the distance is far from the measured region. It is likely that those stray lights can be eliminated by considering the contribution from the edge in the data analysis of the core channels. Also, it is seen that the levels of the reflection alters by the discharge scenarios and the reflectance properties. The stray level is basically higher in the high density scenario, because the beam intensity quenched much greater in the high density discharges.

B. Subtraction of reflection

Figure 9(a) shows CXRS spectrum of Ne at ρ=0.05 with (red curves) and without (black curves) reflection at $R_d/R_s = 25/25$. It is noted that bremsstrahlung background signal and reflection from the divertor emission (cold component) was not included here, though the photon noise originated from the bremsstrahlung was taken into account including the effect of reflection. Here, for a case study, the low density scenario is chosen. The stray light spectrum was added by considering the origin of the stray light shown in Fig. 8. The spectra has a slight sharp component when the reflection is taken into account. This is because the reflection is basically from the edge channel where the temperature is rather low. Typically, the temperature at the edge region (ρ=0.95) is one order of magnitude lower than that of the core.

Figure 9(b) shows the spectrum with photon noise including the effect of enhancement of the background noise due to reflection by a factor of two [6]. Here, the offset of the signal by bremsstrahlung and other noises such as the cold component (emission from the divertor and scrape off layer) were not taken into account. Fitting was conducted with two

different fitting function: single Gaussian function and double Gaussian function. Using the single Gaussian, the deduced temperature was 31.1 $\pm$0.5 keV, which is slightly lower than the actual input temperature of 31.8 keV. When we use the double Gaussian function with the edge temperature of 2 keV, which was assumed to be properly measured, the deduced temperature was 32.0$\pm$0.7 keV, which is closer to the actual input temperature. Although the usage of the double Gaussian function slightly increased the measurement error, it could eliminate the systematic decrease of the temperature due to the stray light originated from the edge.

V. CONCLUSIONS

Ray tracing simulation was conducted to assess the stray light level in divertor impurity monitor (DIM) and charge exchange recombination spectroscopy (CXRS). Transfer matrices were made using ray tracing calculations, and they were used to assess and mitigate the stray light. It was shown that reflected light from the X-point emission could form a phantom peak in the field of views from under the divertor dome, and the stray light level could be greater than 100%. We used three different models with different source allocation to build transfer matrix for mitigation. It was found that better performance was obtained when the sources around the strike points and the X-point were allocated in a detailed manner. Since the emissions from the strike points and the X-point can be strong, the allocation of the sources around those locations are crucial. By applying the mitigation method, it was found that the error caused by the stray light can be decreased by more than an order of magnitude or became comparable to 10%.

Concerning the reflection of the CXRS signal, the stray light level significantly depend on the diffuse reflection component. It was assessed the emission from the edge was the major reflection component for the core signal. We demonstrated that the systematic error in the core field of view caused by the reflection can be subtracted by using the double Gaussian fitting procedure using the temperature obtained at the edge.

Acknowledgements

We thank Dr Andrei Kukushkin for providing us the emission profile. This work was supported in part by a Grant-in-Aid for Scientific Research (B) 15H04229.

The views and opinions expressed herein do not necessarily reflect those of the ITER Organization.

[1] E. M. Hollmann, A. Y. Pigarov and R. P. Doerner: Review of Scientific Instruments **74** (2003) 3984 .

[2] A. Kukushkin *et al.*: EFDA-JET-CP(13)04/05 (2013) .

[3] V. S. Neverov, A. Kukushkin, M. Stamp, A. Alekseev, S. Brezinsek and M. von Hellermann: Nucl. Fusion **57** (2017) 016031.

[4] S. Kajita, E. Veshchev, S. Lisgo, R. Reichle, R. Barnsley, M. Walsh, A. Alekseev, A. Gorshkov, D. Vukolov, J. Stuber and S. Woodruff: Plasma Physics and Controlled Fusion **55** (2013) 085020.

[5] S. Banerjee, P. Vasu, M. von Hellermann and R. J. E. Jaspers: Plasma Physics and Controlled Fusion **52** (2010) 125006.

[6] S. Kajita, M. D. Bock, M. von Hellermann, A. Kukushkin and R. Barnsley: Plasma Physics and Controlled Fusion **57** (2015) 045009.

[7] M. Kocan, R. Reichle, M.-H. Aumeunier, J. P. Gunn, S. Kajita, F. L. Guern, S. W. Lisgo, T. Loarer, A. S. Kukushkin, A. S. Naik, F. Rigollet and B. Stratton: Physica Scripta **2016** (2016) 014047.

[8] M.-H. Aumeunier, M. Kocan, R. Reichle and E. Gauthier: Nuclear Materials and Energy (in press) (2017) .

[9] A. B. Kukushkin, V. S. Neverov, A. G. Alekseev, S. W. Lisgo and A. S. Kukushkin: Fusion Sci. Technol. **69** (2016) 628.

[10] LightTools page. https://optics.synopsys.com/lighttools/ (Date of access: 28/06/2017).

[11] S. Kajita, E. Veshchev, R. Barnsley and M. Walsh: Contributions to Plasma Physics **56** (2016) 837.

[12] S. Kajita, E. Veshchev, S. Lisgo, R. Barnsley, P. Morgan, M. Walsh, H. Ogawa, T. Sugie and K. Itami: Journal of Nuclear Materials **463** (2015) 936 .

[13] R. Reichle, J.-P. Lasserre, F. Oelhoffen, C. Desgranges, F. Faisse, L. Eupherte, C. Pocheau and M. Todeschini: Physica Scripta **2009** (2009) 014029.

[14] A. Kukushkin, H. Pacher, V. Kotov, G. Pacher and D. Reiter: Fusion Engineering and Design **86** (2011) 2865 .

[15] M. Yaala and M. Laurent, in private communication.

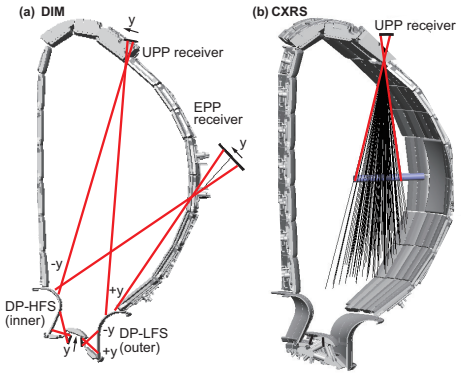

FIG. 1: A schematic of the model of LightTools for (a) divertor impurity monitor and (b) CXRS.

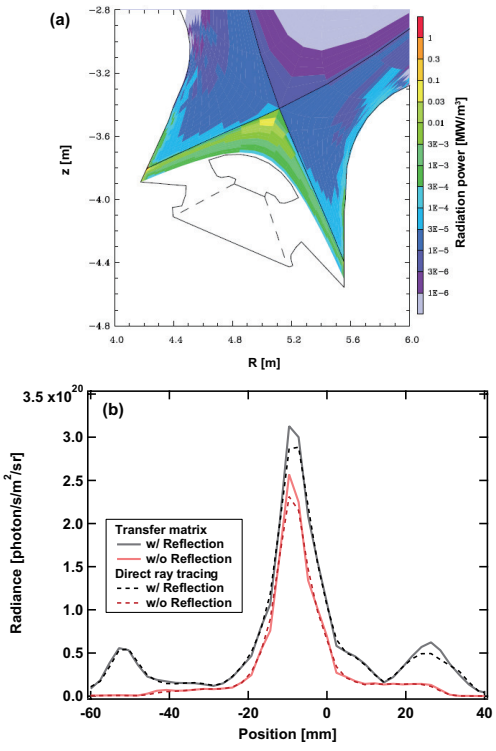

FIG. 2: (a) A profile of calculated He I emission power at 587 nm (2^3P-3^3D) used for this study and (b) a comparison between the results from the direct ray trace calculation and obtained using the transfer matrix for the UPP receiver.

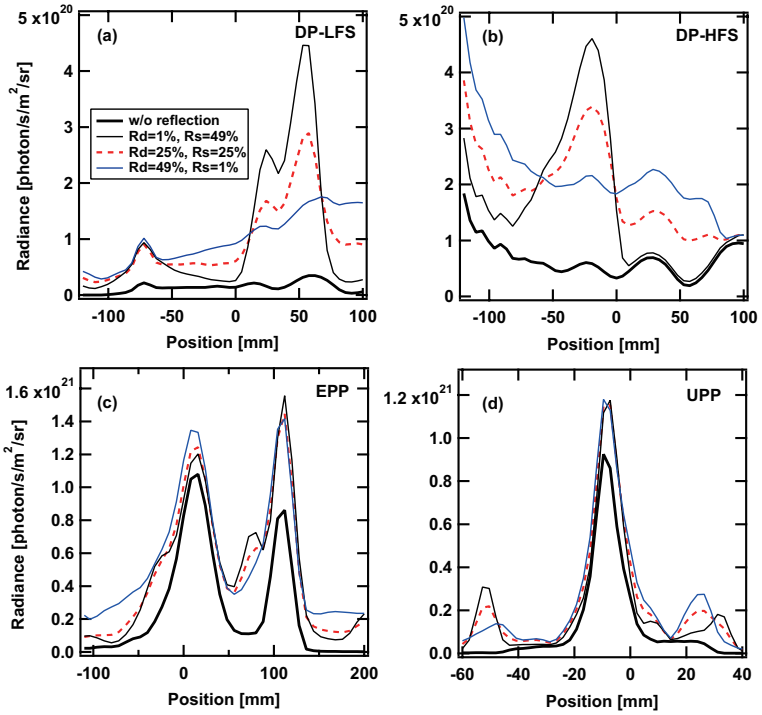

FIG. 3: The calculated radiance profiles of He I (587 nm) for (a) DP-LFS, (b) DP-HFS, (c) EPP, and (d) LPP receivers. The case without reflection, and three cases with reflection for $R_d/R_s = 1/49$, 25/25, and 49/1 are shown.

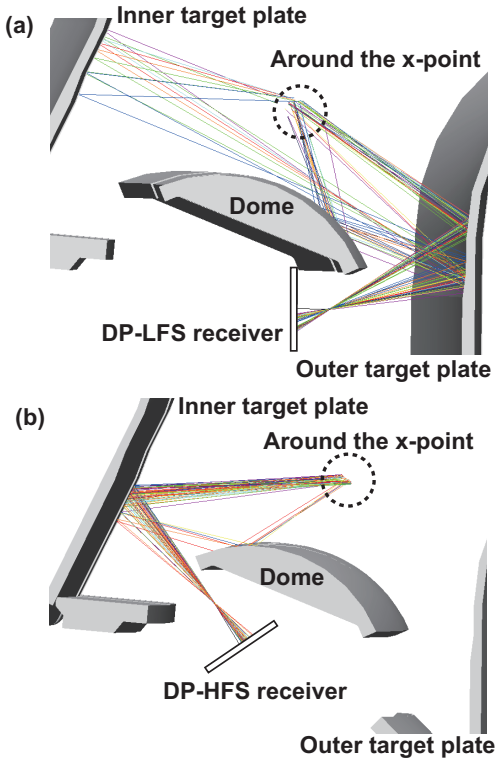

FIG. 4: Major ray paths that contributed to the reflection peaks in case of specular case ($R_d/R_s = 1/49$) for (a) DP-LFS and (b) DP-HFS.

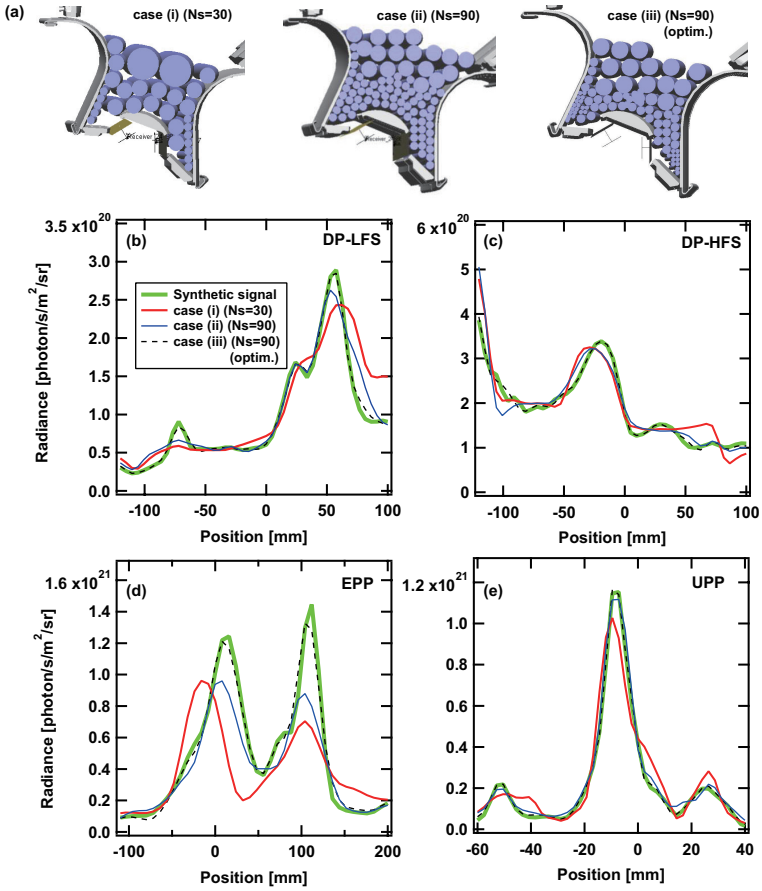

FIG. 5: (a) Schematics of the three model showing the allocation of the sources and comparisons between the synthetic and calculated radiances profiles for (b) DP-LFS, (c) DP-HFS, (d) EPP, and (e) UPP receivers. Green solid lines are the synthetic profiles and red solid, blue solid, and black dotted lines are calculated profiles for cases (i)-(iii), respectively.

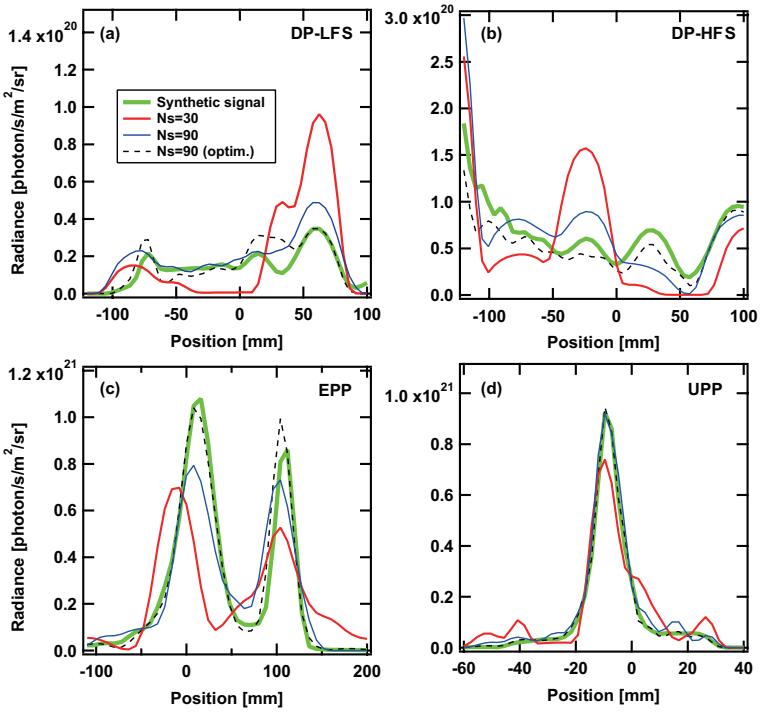

FIG. 6: Comparisons between the synthetic and reconstructed profiles without reflection using source allocations in cases (i)-(iii) for (a) the DP-LFS, (b) DP-HFS, (c) EPP, and (d) UPP receivers.

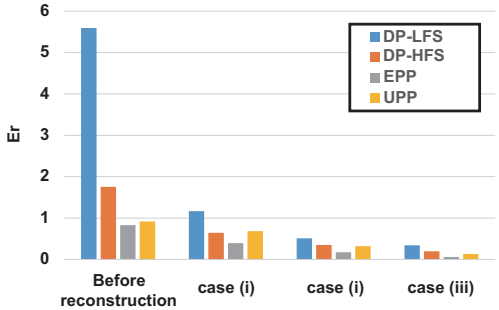

FIG. 7: The error of the each receiver for different source allocation cases, i.e. case (i)-(iii), in addition to the case before the reconstruction.

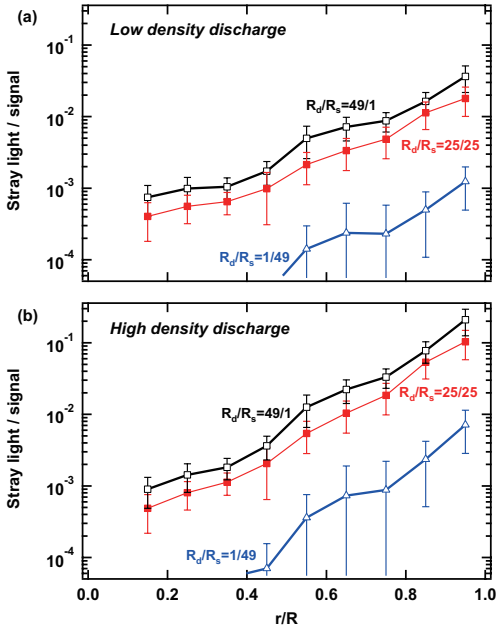

FIG. 8: The profile of the origin of the stray light for the charge exchange signal at $r/R = 0.05$ in (a) low density discharge scenario and (b) high density discharge scenario. Three different reflection properties were chosen for the calculation, i.e., $R_d/R_s = 49/1$, 25/25, and 1/49.

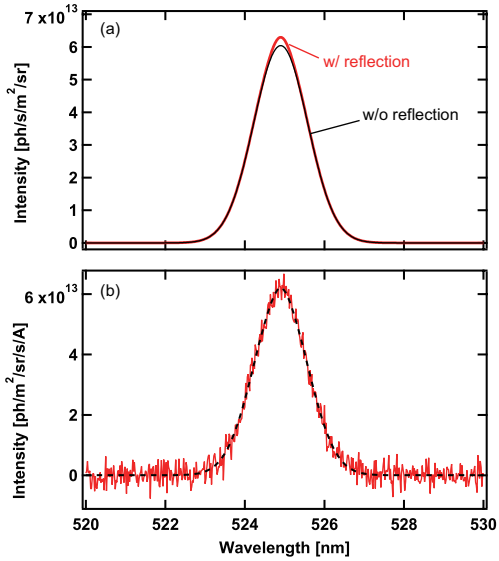

FIG. 9: Typical Spectrum of CXRS Ne signal with (red curves) and without (gray curves) reflection, i.e., stray light, in (a) without photon noise and (b) with photon noise.